1 **Hydrodynamics and sediment deposition in turbidity currents: comparing continuous**

2 **and patchy vegetation canopies, and the effects of water depth**

3

4 Marianna Soler[a], Teresa Serra[a], Andrew Folkard[b] and Jordi Colomer[a]

5 [a] Department of Physics, University of Girona, Girona, Spain

6 [b] Lancaster Environment Centre, Lancaster University, Lancaster, United Kingdom

7

8

9 marianna.soler@udg.edu

10 jordi.colomer@udg.edu

11 a.folkard@lancaster.ac.uk

12 teresa.serra@udg.edu

13

14 *Correspondence:*

15 Marianna Soler

16 c/ Maria Aurèlia Capmany, 61

17 Campus Montilivi

18 17003 Girona

19

21

22

Abstract

A flume experiment was carried out to improve understanding of interactions between turbidity currents and aquatic vegetation canopies and their landscape-scale consequences. It focussed on comparing hydrodynamics and sediment deposition in continuous canopies with those in vegetation patches, and on the effects of varying water depth – both of which are previously unreported. The currents' particulate load was characterised as a mix of fine and coarse fractions. Varying canopy frontal densities, a, and water depths, H, were used. Fifteen runs were carried out with the flume fully vegetated, and a further ten with shorter vegetation patches. In all runs, the currents evolved as expected through inertial, drag-dominated and viscous regimes. The positions at which transitions between the regimes occurred were measured and analysed. In the fully-vegetated runs, both transition positions varied linearly with aH for $aH < 0.8$, and were constant when $aH > 0.8$. We argue that the variation at lower values of aH is caused by non-canopy drag forces becoming non-negligible compared to the canopy drag. An equation is derived that models, as a function of a and H, the size a vegetation patch needs to be for its effect on turbidity currents to be the same as that of a continuous canopy. The sediment depositional flux rate for fine particles from the currents within the vegetation was greater than that for coarse particles, by a factor of 1.57. This suggests that bed sediment deposited within canopy patches by turbidity currents will be on average finer than that in gaps between patches, as has been found previously for currents and waves. Thus, this effect will contribute to the development of inter-tidal and shallow sub-tidal landscapes characterized by patches of dense vegetation and fine sediments, surrounded by bare regions with coarser sediments. Our results imply that the distances over which the phenomena we document occur in typical inter-tidal and shallow sub-tidal contexts are of the same order of magnitude as sizes of patches of saltmarsh plants and seagrasses. This indicates that the reported patch length effects are highly relevant to understanding eco-hydrological interactions in these contexts.

1. Introduction

1.1.   Biophysical interactions in aquatic plant canopies

The effects of aquatic plant canopies on hydrodynamic, sedimentary and geomorphological processes have been studied in many contexts, including seagrass meadows (e.g. Agawin and Duarte, 2002; Folkard, 2005; El Allaoui et al., 2016; Colomer et al., 2017); mangroves (e.g. Nardin et al., 2016; Gillis et al., 2019); saltmarshes (e.g. Adam, 2002; Schulze et al., 2019); in-stream and riparian river vegetation (e.g. Cotton et al., 2006; Lowe et al., 2010; Montakhab et al., 2012; Gurnell, 2014; Licci et al., 2019); and in more general or idealized studies (e.g. Nepf, 1999; Madsen et al., 2001; Zong and Nepf, 2010; Liu and Nepf, 2015; Manners et al., 2015; Zhang et al., 2018). They have been found widely to act as ecosystem engineers (e.g. Ludwig et al., 2005; Nepf, 2012), profoundly altering landscape evolution via biophysical interactions at multiple scales (Folkard, 2019). Understanding these interactions and their consequences is therefore crucial for understanding the functioning of coasts, lakes and rivers.

In recent years, because of climate change and other anthropogenic stresses, aquatic plant canopies have become increasingly degraded, through either fragmentation (Adam, 2002; Tamburello et al., 2012) or reduction of the area they cover (Richardson et al., 2007; Colomer et al., 2017; Dwirea et al., 2018; Serra et al., 2018; Xiu et al., 2019). For this reason, research into their biophysical interactions has recently focussed on fragmented and finite-sized canopies (Zong and Nepf, 2010; El Allaoui et al. 2015, 2016; Zhang et al., 2018).

Most studies of biophysical interactions of fragmented aquatic vegetation canopies have considered their interactions with uni-directional flows. In this context, one of the main ways in which vegetation canopies engineer their physical environment is through reducing bed erosion (Madsen et al., 2001) and increasing deposition of sediment (Agawin and Duarte, 2002; Montakhab et al., 2012; Zong and Nepf 2010). This triggers a positive feedback, as retention of fine sediment - which is rich in organic material and nutrients - by the vegetation promotes the expansion of the vegetated region (Gurnell, 2014). A minimum patch size and minimum stem

82   density within a patch of vegetation is required for it to have the capability to engineer its physical

83   environment in this way (Licci et al., 2019), and to produce a positive feedback for the vegetation

84   (Bouma et al., 2009). Deposition of sediment within vegetation canopies is dependent on the

85   mean flow speed and the characteristics of the vegetation (Liu and Nepf 2015). Hence, as well

86   as completely fragmented canopies having sediment dynamics that are dependent on their spatial

87   structure, this is also the case in continuous canopies in which plant properties such as stem

88   diameter, flexibility and density are spatially heterogeneous (e.g. Schulze et al., 2019). Thus, the

89   hydrodynamics of heterogeneous canopies depend on variations of canopy characteristics at both

90   the patch- and meadow-scale (Adhitya et al., 2014).

91

92   The interactions of vegetation canopies and uni-directional flows may also produce negative

93   feedbacks, for example when the enhancement of flow speed adjacent to lateral patch edges

94   produces scouring which inhibits plant growth and patch development (Schoelynck et al., 2012;

95   Bouma et al., 2013). Differences in patch diameter, inter-patch distances and plant densities have

96   been found to produce differences in velocity flow structures around patches. For example, both

97   the amount of flow acceleration around patches and the lateral distance from the patch to the

98   point where maximum flow acceleration occurs increase with increasing patch size

99   (Vandenbruwaene et al., 2011).

100

101   The presence of scale-dependent feedbacks such as these create self-organised heterogeneity

102   in landscapes and are key mechanisms responsible for shifts between unvegetated and

103   vegetated landscape states (Bouma et al., 2009). They have important implications for ecosystem

104   functioning, such as increased ecosystem productivity and increased resilience and resistance to

105   environmental change (Rietkerk and van de Koppel, 2008).

106

107   El Allaoui et al. (2015, 2016) and Colomer et al. (2017) extended studies of hydrodynamic

108   interactions with heterogeneous vegetation canopies to consider waves. As with the work cited

109   above, they found that the spatial scale of variations (patch and gap size) and canopy

110   characteristics (stem density) to be the most important factors determining wave transformations,

111   levels of turbulent kinetic energy and therefore sediment dynamics.

112

113   To date, there has been little work on biophysical interactions between heterogeneous or

114   fragmented vegetation canopies and a third hydrodynamic phenomenon (beyond the uni-

115   directional currents and waves discussed above), namely gravity currents. In the context of

116   considering canopies' effects on sediment dynamics and thus the sort of feedbacks described,

117   the most pertinent forms of gravity currents are those driven by suspended particle concentration,

118   namely turbidity currents. Soler et al. (2017, 2020) considered the interactions of turbidity currents

119   with continuous, uniform vegetation canopies and the effects of varying turbidity current

120   particulate concentration, canopy density and vegetation type. Here, we extend this work by

121   investigating for the first time the effects of water depth on turbidity current-vegetation patch

122   interactions, and the hydrodynamics and sediment deposition patterns of turbidity currents in

123   finite-length patches of vegetation, such as would be found in fragmented canopies.

124

125   *1.2.   Gravity current hydrodynamics*

126

127   Gravity current hydrodynamics have been studied for many years both theoretically (Benjamin,

128   1968) and experimentally (Simpson, 1982; Shin et al., 2004). The most common approach used

129   in experimental studies has been lock-exchange flume experiments, in which two fluids of different

130   densities (usually generated by salt dissolution) are initially at rest in a flume and separated from

131   each other by a lock gate. When the gate is removed, differences in the hydrostatic pressure

132   cause the denser fluid to flow as a gravity current beneath the less-dense fluid, along the bottom

133   boundary of the flume, forcing the less-dense fluid to flow in the opposite direction over the denser

134   fluid. As the gravity current flows along the flume, it passes through three regimes (e.g. Huppert

135   and Simpson 1980; Maxworthy et al. 2002), see Table 1. In the first – known as the 'inertial regime'

136   – the current proceeds as if released from an infinite reservoir, and the position of the front of the

137   current (hereinafter referred to as the 'current toe', following Tanino et al., 2005), x_c, varies in

138   direct proportion to time, t, and depends on the reduced gravity, g', and water depth, H (Tanino

139   et al., 2005). When the lock gate is removed, it generates an interfacial wave that propagates in

140   the opposite direction to the gravity current until it reflects off the back wall of the flume. This

141   reflected wave then flows in the same direction as the gravity current and at the point it catches

142   up with the current toe, the second regime begins. In this 'self-similar regime', the current motion

143   is determined by a balance between buoyancy and inertial forces, and the flow slows over time

144   such that the position of the toe varies as $t^{2/3}$ (Maxworthy et al. 2002). However, if the current is

145   propagating through an array of obstacles (for example, simulated or natural vegetation), it

146   evolves instead from the inertial regime to a 'drag-dominated regime' (e.g. Tanino et al., 2005; La

147   Rocca et al., 2008; Zhang and Nepf, 2008, 2011; Gonzalez-Juez et al., 2010; Nogueira et al.,

148   2013, 2014; Bhaganagar 2014; Soler et al., 2017, 2020). Here, the gravity current is affected by

149   the drag due to the obstacles, which dominates over both inertial forces and the drag forces

150   caused by the flume bed and sidewalls. In this regime, the speed of the current toe reduces more

151   than in the self-similar regime found in obstacle-free cases, varying from $x_c \propto t^{2/3}$ to $x_c \propto t^{1/2}$

152   (Hatcher et al. 2000).

153

154   In order to quantify the drag forces due to an array of obstacles, it is necessary to calculate its

155   drag coefficient, C_{Da}. For randomly-distributed arrays of vertical cylinders (often used to simulate

156   plant stems), Ghisalberti and Nepf (2004) found that

157

158                $C_{Da} = C_D / \{1.16 - 9.31ad + 38.6(ad)^2 - 59.8(ad)^3\}$ (1)

159

160   where $a = Nd/A$ is the frontal area of the cylinders per unit volume (Nepf, 1999), N is the number

161   of stems, d is stem diameter and A is the bed area over which the N stems are distributed. C_D is

162   the drag coefficient associated with the individual obstacles (which are assumed to be cylinders),

163   and is a function of the cylinder Reynolds number $Re_c = ud/\nu$, where ν is the kinematic viscosity

164   of the fluid, and u the speed of the current toe, such that $C_D = 1 + 10 Re_c^{-2/3}$ (White, 1991). This

165   expression for C_D applies for Re_c values ranging from 1 to 10^5 and dimensionless array densities

166    $ad < 0.03$ (Nepf, 1999). Note that this implies that the drag coefficient of a randomly-distributed

167   array of obstacles in a flume will increase as a gravity current travels along the flume due to the

168   reduction in the velocity of the gravity current.

169

170   The third and last regime through which gravity currents pass is called the 'viscous regime' and

171   occurs when the current has spread so far that it has become thin enough for viscous forces

172   between the two fluids to become important and overcome the inertial forces. In this regime, the

173   speed of the current toe reduces until its position varies as $x_c \sim t^{1/5}$.

174

175   *1.3.   Turbidity currents*

176

177   Turbidity currents are gravity currents in which the density-varying agent is the concentration of

178   particles in suspension. Their dynamics can be more complicated than those of gravity currents

179   in which the density-varying agent is conservative on the timescale of the current's development,

180   for example heat or salt concentration. This is because of sediment loss due to deposition and/or

181   sediment entrainment due to bed scouring, which change the density difference that drives the

182   current, altering its temporal evolution (Francisco et al., 2017). Bonnecaze et al. (1993) found that

183   the position of the toe of a turbidity current of finite volume spreading over a rigid, unobstructed

184   horizontal surface in shallow water, evolved following $x_c \propto t^{2/3}$ (Table 1). The spatial and temporal

185   evolution of turbidity currents is dependent on their grain-size distribution, that is, the ratio

186   between the amounts of fine and coarse particle they carry (Felix 2002). Currents dominated by

187   fine particles travel over larger distances, which results in sedimentation further downstream than

188   in currents dominated by coarse particles (Harris et al., 2002). Moreover, the runout distance to

189   which coarse particles are transported by turbidity currents increases substantially when the

190   proportion of fines in the turbidity current is increased (Gladstone et al., 1998).

191

192   In natural environments, turbidity currents are often observed travelling, or to have travelled,

193   through arrays of obstacles. One example of this is turbidity currents flowing through aquatic

194   vegetation canopies. In experiments investigating this configuration, Soler et al. (2017) found that

195   the controlling factor in the temporal evolution of the current toe position was the canopy drag.

196   They also compared their results to experiments studying a salinity-driven gravity current passing

197   through an array of obstacles (Hatcher et al., 2000) and found that, although $x_c \propto t^{1/2}$ in both

198   cases, the effect of depositional loss of sediment particles from the turbidity current was a

199   reduction of 70% in the constant of proportionality in this relationship.

200

201   As noted above, studies of turbidity currents' interactions with arrays of obstacles or vegetation

202   canopies to date have focussed on cases where the array or canopy is continuous and uniform.

203   Cases where the vegetation canopy is of finite extent have not previously been considered. This

204   leaves open the questions of how the size of finite patches affects their influence on turbidity

205   current hydrodynamics and sediment transport processes, and specifically how long vegetated

206   patches need to be to provide dynamic effects equivalent to those of continuous vegetated

207   canopies – the equivalent question to that addressed by Licci et al. (2019) for vegetation patches

208   in uni-directional flows in rivers. These questions are addressed in the present study, by

209   measuring the effects on current hydrodynamics and sediment deposition of vegetation patches

210   that end at different points within the currents' evolution through the three dynamic regimes

211   described above, and comparing them to the effects of continuous vegetation canopies.

212

213   **2.   Material and methods**

214

215   *2.1.   Experimental set-up*

216

217   The experiment was conducted in a methacrylate flume (4.0 m long, 0.3 m high and 0.3 m wide)

218   that was separated into two sections with a removable vertical lock gate (Figure 1). The shorter

219   reservoir section was filled with a mixture of sediment and water that would create the turbidity

220   current, while the longer section was filled with water only. The longer experimental section was

221   populated with vertical PVC dowels with a diameter of 6 mm, forming a generic model of an

222   emergent canopy of rigid-stemmed plants. To construct the model canopy, a PVC base sheet

223   was perforated at positions selected using a random number generator, following Pujol et al.

224   (2013), and a single dowel secured in each hole. The density of vegetation canopies (real or

225   simulated) can be quantified using various parameters. Commonly, solid plant fraction (SPF) is

226   used. This is defined as the percentage of the bed area occupied by vegetation stems, SPF =

227    $100n\pi(d/2)^2$, where n is the number of stems per unit bed area and d the stem diameter (Pujol et

228   al., 2010). Here, runs were carried out with canopy density values from SPF = 1%, (356 plants m^{-}

229   ^{2}), to 4%, i.e. (1424 plants m^{-2}), as well as a control run without plants (SPF = 0%). Canopy density

230   is also quantified using $a = nd$, the canopy frontal area per unit bed area (or simply "frontal area

231 density"), or the dimensionless array density, ad (= SPF/25π). Values of all of these parameters

232 for each experimental run are shown in Table 2. Note that the values of ad varied from 0.013 to

233 0.051, and all fall within the range observed in natural vegetation canopies (Bouma et al., 2007).

234

235 *2.2.   Preparation of the turbidity current fluid*

236

237 The flume was filled with water to a height H the day before each run to allow the water

238 temperature to equilibrate. The lock gate was then lowered into position, separating the two

239 sections. To generate the turbidity current, 3L of water was taken from the reservoir section

240 (Figure 1) and to it was added the mass of sediment needed to produce an initial concentration

241 of C_0 = 6 gL^{-1} throughout the whole of the reservoir. The sediment-water mixture was stirred

242 vigorously for five minutes to ensure a homogeneous sediment suspension, and then returned to

243 the reservoir section and mixed thoroughly.

244

245 The sediment was taken from the Pletera ponds at the Empordà Marshes Natural Park in NE

246 Spain, in order to provide natural sediment characteristics. The collected sediment was first

247 cleaned, removing leaves and roots and then sieved to remove particles larger than 0.5 mm. The

248 particle size distribution of the remaining sediment was measured with a LISST-100 particle size

249 analyser (Sequoia Scientific, Inc., Bellevue, WA, USA). It was found to have a bimodal size

250 distribution (Figure 2): 79.0% of the mass was made up of particles with diameters ranging from

251 6.2 to 104 μm (coarse fraction), 17.9% was made up of particles with diameters ranging from 2.2

252 to 6.2 μm (fine fraction). The coarse fraction fell into the category of weakly cohesive particles

253 (fine to coarse silts and small sand particles) and the fine particles into the category of very

254 cohesive particles (clays and very fine silts), according to the classification of Van Rijn (2007) and

255 Blott and Pye (2012). The remaining 3.1% of the sediment volume consisted of only a few

256 particles with larger volumes, which quickly settled out of the turbidity currents and therefore were

257 not considered in the analysis.

258

259 *2.3.   Simulated Vegetation Patches and Experimental Run Parameter Values*

260

261   Twenty-five experimental runs, all with an initial concentration C_0 = 6.0 gL^{-1}, were carried out,

262   Parameter values for each run are shown in Table 2. Firstly, in addition to a control run with no

263   vegetation (Run 1), fourteen runs (Runs 2-15) were carried out with the whole 280 cm length of

264   the flume's experimental section populated with simulated vegetation, so that the patch length,

265   L_{patch}, was in effect 280 cm. These were designed to investigate the influence of varying water

266   depth and canopy density on the downstream distances at which the turbidity currents underwent

267   the dynamic regime transitions described above, whilst they were within the vegetation canopy.

268   Therefore, water depth and canopy density were varied from run to run, using values of H = 3, 6,

269   9, 12 and 15cm, and SPF = 1, 2, 2.5, 3, 3.5 and 4% respectively. Subsequently, ten runs (Runs

270   16-25) were carried out in which the patches of simulated vegetation were shorter. In these, two

271   water depths (H = 6 and 12 cm) were used, and the canopy density was held constant at SPF =

272   4%. The shorter patch lengths were chosen such that they ended at different points in the dynamic

273   evolution of the turbidity current in the run in which L_{patch} = 280 cm, SPF = 4% and H = 12cm (Run

274   7, Table 2), the maximum value of each parameter. Five different patch lengths were chosen: one

275   which ended within the inertial regime; three ending within the drag-dominated regime; and one

276   extending into the viscous regime.

277

278   Thus, the experimental configuration was characterized by three parameters: the vegetation

279   canopy length, L_{patch} [m], the water depth, H [m], and the frontal area per unit volume, a [m^{-1}],

280   which quantified the canopy density, with the turbidity current's characteristics held constant.

281   From these, we constructed two non-dimensional parameters, which we used as the independent

282   variables in our analyses: L_{patch}/H, the aspect ratio of the vegetation canopy; and aH (= NdH/A),

283   the canopy frontal area per unit bed area. The values of these for each run are shown in Table 2.

284   The ranges over which runs are distributed are 5.8 ≤ L_{patch}/H ≤ 93.3 and 0.13 ≤ aH ≤ 1.27 (and

285   the control case, for which $L_{patch}/H = aH$ = 0).

286

287   *2.4.   Development of the turbidity current*

288

289   Once the sediment-water mixture had settled in the reservoir section of the flume, the lock gate

290   was released, allowing it to flow as a turbidity current into the experimental section. In all runs,

291   the initial (inertial regime) speed of the current toe was two to three orders of magnitude greater

292   than the settling velocity of the coarse particles, and three to four orders of magnitude higher than

293   settling velocities of the fine particles. Thus, the current was considered to be conservative in this

294   stage of its evolution, i.e. the density anomaly driving the current remained constant.

295

296   A moving CCD video camera was situated at the top of the flume (Figure 1A) to determine the

297   position and speed of the current toe. Its position, x_c, was located on the video images using edge

298   detection (parallax error was less than 3% and was not corrected for) and measured on a scale

299   with 0.1 cm gradations mounted on the flume bed. In all runs, the obscuration of the line of sight

300   by the dowels was not enough to affect the view of the current toe. The toe speed was calculated

301   from the position and time data recorded on the video footage of its progression down the flume.

302   Following previous studies (Tanino et al., 2005; Soler et al., 2020) we converted the toe position

303   into the non-dimensional parameter $C_{Da}ax_c$, and used this in our analyses of the current's

304   hydrodynamic progression down the flume. This parameter is a measure of the drag force due to

305   the vegetation normalized by the inertial force of the current at its toe. Hence, we refer to it

306   hereafter as the 'normalized toe drag'.

307

308   In order to analyse the pattern of sediment deposition from the turbidity current, fourteen

309   sediments traps (ST0 to ST13) were located along the flume bed. The first one (ST0) was located

310   in the reservoir section, 20 cm upstream of the lock gate. The other thirteen (ST1-ST13) were

311   evenly distributed along the flume bed at intervals of 20 cm, starting 20 cm to the right of the lock

312   gate and finishing 10 cm from the far end of the flume. Each trap had a volume of 21.3 mL^{-1} and

313   was inserted into the PVC base without extruding above the flume bed, to avoid any interference

314   with the passage of the turbidity current (Figure 1B).

315

316   When the turbidity current arrived at the end of the canopy, all the traps were covered manually

317   with lids to avoid collection of sediment that settled out of the current after it had been reflected

318   by the end wall. In order to avoid overestimation of the amount of sediment captured by the traps

319   further upstream caused by the longer time of sedimentation, the effective time that each ST was

320   collecting sediment was recorded in each run. The sediment collected in each trap was analysed

321 with the LISST-100 (following Serra et al. 2002, 2005), which gave the volume occupied by

322 particles in each of 32 size classes logarithmically distributed in the range 2.5 to 500 μm. Because

323 the major sediment constituent in all the traps was silt particles (79%), the particle volume

324 concentration (μL/L) was transformed into deposited sediment mass by assuming that the density

325 of the particles was 2.798 gcm^{-3}, the standard value for silt particle density (Mandal and Maiti,

326 2015). No flocculation of fine sediment was observed, so its potential effects were not taken into

327 account in this conversion. The deposited mass per unit bed area was then converted to a

328 depositional flux at each sediment trap by dividing by the time over which the deposition occurred.

329 This value was divided by the initial horizontal flux of sediment carried by the current as it emerged

330 from the reservoir, giving a non-dimensional depositional flux rate, DF, for each trap.

331

332 **3.   Results**

333

334 *3.1.   Turbidity current evolution within fully-vegetated canopies*

335

336 The temporal evolution of the current toe position, x_c, in the fully-vegetated runs was dependent

337 on the canopy density: in general, as the canopy increased, the toe speed reduced (Figure 3).

338 Initially in all runs (until approximately $t = 30$ s), the turbidity current was in the inertial regime, as

339 x_c varied linearly with time (i.e. the flow speed was constant). In the non-vegetated case (SPF =

340 0%), after the inertial regime, the flow slowed down, taking on a time dependence $x_c \propto t^{2/3}$, while

341 the deceleration was greater in the vegetated runs. The evolution of x_c in Run 6 is shown in Figure

342 4A as an example of transition from the inertial regime ($x_c \propto t^1$) to the drag-dominated regime (x_c

343 $\propto t^{1/2}$) and finally to the viscous regime ($x_c \propto t^{1/5}$). The positions at which these regime transitions

344 occurred are referred to hereafter as $x_c = L_{ini}$ (the position at which the current transitions from the

345 inertial regime, and the drag-dominated regime is initiated) and $x_c = L_{end}$ (the position at which the

346 drag-dominated regime ends and the viscous regime begins).

347

348 The normalized toe drag was calculated for L_{ini} and L_{end} in each of the fully-vegetated runs. Given

349 that L_{patch}/H was constant across these runs, the relationships of $C_{Da}aL_{ini}$ and $C_{Da}aL_{end}$ to the other

350   independent variable defined above, aH, were investigated, and plotted in Figure 4B. Both varied

351   linearly with aH for $aH < 0.8$, following

352

353         $$C_{Da}aL_{ini} = 7.13aH + 1.32 \qquad (2)$$

354

355   ($r^2 = 0.87$; n = 10; p < 0.001) and

356

357         $$C_{Da}aL_{end} = 12.24aH + 3.92 \qquad (3)$$

358

359   ($r^2 = 0.97$; n = 10; p < 0.001), respectively. When $aH > 0.8$, both were constant at $C_{Da}aL_{ini} = 7.1 \pm$

360   0.2 and $C_{Da}aL_{end} = 13.1 \pm 0.2$, respectively.

361

362   *3.2.   Turbidity current evolution in finite-length vegetation patch runs*

363

364   As noted above, values of $C_{Da}aL_{ini}$ and $C_{Da}aL_{end}$ from Run 7 were used to determine the lengths

365   of the vegetation patches in the finite-length patch runs. In Run 7, $aH = 1.02$, so $C_{Da}aL_{ini} \approx 7$ and

366    $C_{Da}aL_{end} \approx 13$. Patch lengths were thus chosen for Runs 16-25 such that $C_{Da}aL_{patch} = 6, 8, 10, 12$

367   and 14, using each in one run with $H = 12$ cm and another with $H = 6$ cm (Table 2). The $C_{Da}aL_{patch}$

368   = 6 patch (Runs 20 and 25) ended in the inertial regime of Run 7; the $C_{Da}aL_{patch} = 8, 10$ and 12

369   patches (Runs 17-19 and 22-24) ended in the drag-dominated regime of Run 7; and the $C_{Da}aL_{patch}$

370   = 14 patch (Runs 16 and 21) ended in the viscous regime of Run 7.

371

372   In qualitative terms, the evolution of the currents proceeded as expected. In Runs 16 and 21, both

373   L_{ini} and L_{end} occurred within the vegetation, so the current underwent its full evolution and reached

374   the viscous regime within the vegetation, behaving as if in a continuous, infinite-length canopy

375   (Figure 5C). In runs 17-19 and 22-24, L_{ini} occurred within the vegetation, but the current emerged

376   from the patch in a drag-dominated state and subsequently transitioned to a viscous regime

377   downstream of the patch, apparently without changing to a self-similar state (in which $x_c \propto t^{2/3}$

378   would have been observed) despite the absence of vegetative drag (Figure 5B). Here too,

379   therefore, the current behaved as if in a fully-vegetated, continuous canopy, transitioning to a

380   drag-dominated state rather than a self-similar state. In runs 20 and 25, the vegetation patch

381   ended upstream of L_{ini}, so the current was still in the inertial regime as it emerged from the patch

382   and evolved as if it were flowing in a non-vegetated flume, passing through self-similar ($x_c \propto t^{2/3}$)

383   and viscous regimes (Figure 5A).

384

385   Quantitatively, and surprisingly, L_{ini} had a consistent relationship with aH and L_{patch}/H, regardless

386   of whether the regime transitions occurred within the patch or downstream of it. This is shown in

387   Figure 6, in which data from both the fully-vegetated and finite patch runs all fall on a line with

388   both axes in log form, that means there is a power law relationship given by

389

390    $$\frac{L_{ini}}{H} = 3.721 \left[(aH)^{0.64} \left(\frac{L_{patch}}{H} \right)^{-0.30} \right]^{-0.77} \tag{4}$$

391

392   *3.3.   Sediment deposition from turbidity currents in vegetation patches*

393

394   We focussed our analysis of sediment deposition on the drag-dominated regime of the currents'

395   evolution. *DF* values were selected from the sediment trap that was positioned closest to the

396   middle of the drag-dominated region in each run. These were taken to be representative of the

397   sediment deposition across the whole drag-dominated regime and, because that regime occurred

398   in between the inertial and viscous regimes, to be also representative of the sediment deposition

399   from the turbidity current as a whole. As for the hydrodynamic data, the *DF* values were analysed

400   in relation to *aH* and L_{patch}/H. The results of this analysis are shown in Figure 7, in the form of

401   plots of *DF*/*aH* against L_{patch}/H. Across all runs, for both fine and coarse particles, *DF*/*aH* was

402   approximately constant when $L_{patch}/H < 20\pm2$, and increased with increasing L_{patch}/H, following a

403   power law relationship, above this threshold value (Figure 7).

404

405   The behaviour of *DF* differed for coarse and fine particle fractions. For $L_{patch}/H < 20\pm2$,

406

407    $$DF_{fine} = 0.758aH \tag{5}$$

408

409 (n=24, 95% confidence interval [0.631, 0.885]) for fine sediment and

410

411 $$DF_{coarse} = 0.475aH \qquad\qquad\qquad (6)$$

412

413 (n=23, 95% confidence interval [0.359, 0.592]) for coarse sediment. This implies a fine-to-coarse

414 flux ratio, DF_{fine}/DF_{coarse}, of 0.767/0.489 = 1.60. For $L_{patch}/H > 20\pm2$, the value of DF/aH increases

415 with increasing patch length for both fine and coarse fractions, i.e. the rate of deposition was

416 greater in these longer patches than it would have been in shorter patches of the same density.

417 But the rate of fine particle deposition continued to be greater than that of coarse particle

418 deposition. This difference reduced towards unity as patch length increased, but only slowly, such

419 that when $L_{patch}/H = 88.5$ (the maximum value used here), it was approximately 1.34.

420

421 **4.   Discussion**

422

423 *4.1 Agreement with previous studies*

424

425 The time evolution of turbidity currents flowing through different distributions of vegetation were

426 studied. In the non-vegetated control case (Run 1), the particles settling out of the current caused

427 a reduction of its density anomaly as it progressed forward, causing a reduction of the current toe

428 speed. Thus, after the initial inertial regime ($x_c \propto t^1$), the position of the current toe followed the

429 time dependence, $x_c \propto t^{2/3}$, found by Bonnecaze et al. (1993) for the same flow configuration. In

430 the runs in which the turbidity current flowed through continuous vegetation, for all vegetation

431 density and water height combinations tested, the pattern of evolution of the current dynamics

432 was found to be in agreement with previous studies (Hatcher et al., 2000; Tanino et al., 2005;

433 Zhang and Nepf, 2008). That is, the turbidity current developed initially in the inertial regime, as

434 in the non-vegetated case, but soon transitioned to a drag-dominated regime, where it was further

435 slowed by the vegetation drag, so that the position of the current toe followed $x_c \propto t^{1/2}$, and

436 subsequently reached a viscous regime where $x_c \propto t^{1/5}$.

437

438 *4.2 Effects of water depth on regime transition positions*

15

440   Unlike previous studies (Soler et al., 2017, 2020), the experiment reported here investigated the

441   effect on turbidity currents of varying water depth as well as canopy density. This revealed that

442   there is a threshold value of the non-dimensional parameter aH, above which the non-

443   dimensionalized positions at which turbidity currents transition from being inertially-dominated to

444   drag-dominated ($C_{Da}aL_{ini}$), and subsequently from being drag-dominated to dominated by viscous

445   forces ($C_{Da}aL_{end}$), are constant. This threshold value was found to be $aH = 0.8$, above which

446    $C_{Da}aL_{ini} = 7.1 \pm 0.2$, and $C_{Da}aL_{end} = 13.1 \pm 0.2$. The former agrees with Tanino et al. (2005) and Soler

447   et. al (2020), who found that $C_{Da}aL_{ini} \approx 7$ remained the case up to $aH = 2.3$, compared to a

448   maximum value of 1.27 in this study. When $aH < 0.8$, both $C_{Da}aL_{ini}$ and $C_{Da}aL_{end}$ decreased linearly

449   with decreasing aH. This is consistent with an explanation that considers the relative influence of

450   drag forces due to the canopy elements compared to other drag forces, including those due to

451   bed shear stress and interfacial stresses between the turbidity current and its overflowing counter

452   current. Note, first, that small values of aH imply vegetation canopies that are either sparse or in

453   shallow water, or both. In shallow water, sparse canopy cases, the drag forces not due to the

454   canopy will have relatively significant influence, meaning that drag forces are greater than

455   predicted by models that only consider the canopy drag (such as that formulated by Tanino et al.,

456   2005, who originally devised the normalised toe drag parameter) and therefore regime transitions

457   will happen earlier than predicted by those models, as found here. If either canopy density or

458   water depth are increased, the non-canopy drag forces become less significant, so the canopy

459   drag-based model fits the data better. Our findings, as illustrated in Figure 4B, suggest that this

460   effect is manifested in the change of relationship at $aH = 0.8$ shown.

461

462   *4.3. Patch length vs. regime transition distances*

463

464   From the empirical relationship found in these data between L_{ini}/H, aH and L_{patch}/H (Equation 4),

465   setting $L_{ini} \leq L_{patch}$ gives

466

467            $$L_{patch} \geq 5.51 a^{-0.636} H^{0.364} \tag{7}$$

468

469   This inequality gives the patch lengths for which the transition to the drag-dominated regime will

470   occur within a vegetated patch, and thus the patch length required to have the same effect on the

471   position of turbidity currents' transition to the drag-dominated regime as a continuous vegetation

472   canopy. From (7), this patch length is only weakly dependent on H and close to being directly

473   proportional to the reciprocal of a. If L_{patch} is shorter than this threshold, the current will emerge

474   from the patch still in its inertial regime and therefore transition to a self-similar regime rather than

475   a drag-dominated one.

476

477   Thus, the results presented here corroborate previous findings that denser canopies cause

478   turbidity currents to transition earlier into the drag-dominated regime. If the vegetated patch is

479   denser (increased a), the turbidity current experiences higher vegetative drag and consequently

480   a smaller patch length is required to cause this transition. To give some indications of the

481   threshold patch length scales that our results imply, sparse patches (say, $a = 2$ m^{-1}) developing

482   in shallow water, with a characteristic depth of, say, 10 cm, need to be at least 1.54 m in length

483   to cause turbidity currents to transition to a drag-dominated state in the same way as a continuous

484   canopy would, while in denser patches (say, $a = 10$ m^{-1}) in the same water depth, a patch length

485   of 0.55 m would be enough for this to occur. In deeper water (say, $H = 1$ m), the same sparse

486   patches would need to have a length of 3.54 m to cause the transition at the same point as a

487   continuous canopy, while in the same denser patches the required length would be 1.26 m. For

488   exemplar, common saltmarsh species *Arthrocnemum fruticosum* (glasswort) and *Juncus*

489   *maritimus* (sea rush), for which canopy densities of $a= 3.64$ m^{-1} and 4.69 m^{-1} have been reported

490   respectively (Soler et al., 2020), in water of 0.5 m depth, the threshold patch lengths would be

491   1.88 m and 1.60 m, respectively. These patch lengths are all of the same order of magnitude as

492   the typical size of patches of vegetation found in salt marsh pioneer zones and seagrasses.

493

494   *4.4. Sedimentation patterns from turbidity currents in degraded vegetation canopies*

495

496   Soler et al. (2020) found that, when turbidity currents flow through fully vegetated canopies,

497   coarse particles initially settle faster than fine particles, leaving the finer particles to be dominant

498   in the material deposited in canopy interiors, thus 'muddifying' them. In agreement with this, here

499   we find the rate of fine particle deposition is higher than the rate of coarse particle deposition once

500   the current has entered significantly into the vegetation and transitioned to a drag-dominated state

501   (Figure 7). At patch lengths such that $L_{patch}/H < 20\pm2$, the ratio of fine to coarse deposition rates

502   is constant with respect to L_{patch}/H at $DF_{fine} = 1.60DF_{coarse}$. Above this threshold, the ratio changes,

503   but only slightly. Keeping in mind that the distribution of patches is often affected by geology and

504   topography, these fine sediments, which are often enriched in nutrients (Vandenbruwaene et al.,

505   2011) will result in a positive feed-back, as evidenced by previous observations. For example, Di

506   Carlo et al. (2005) found that in shallow, well-lit waters, seagrass establishment was densest in

507   nutrient-rich sediments zones and Nardin et al. (2016) found mangroves in Mekong delta

508   expanded as continuous coverage in areas of high sediment availability, but as sparse patches

509   in areas of low sediment supply. Thus, this process will favour a shaping of the landscape-scale

510   canopy structure into patches growing on relatively nutrient-rich, fine sediment, separated by gaps

511   with relatively coarse, nutrient-poor sediment. This is redolent of the structure observed in, for

512   example, chalk streams occupied by patches of *Ranunculus* (Cotton et al., 2006), where the flow

513   carrying the sediment is driven by the component of gravity forcing it down the longitudinal slope

514   of the stream channel, rather than the buoyancy forces driving the turbidity currents studied here.

515

516   Studies on the role of patch size in the ecosystem engineering capacity of submerged plants have

517   also found that patch size affects patterns of sedimentation within them. Schoelynck et al. (2012)

518   used mimic and transplantation experiments in a small river to show that the longer patches were,

519   the more effectively they slowed the current, enhancing sedimentation. Licci et al. (2019) showed

520   that there is a threshold length that river vegetation patches need to attain in order to induce

521   modifications to flow and sedimentation patterns, and that this threshold value differs depending

522   on environmental conditions such as flow velocity. At low velocity sites (0.13 ± 0.01 ms^{-1}), they

523   found that a patch with a length > 0.3 m modified the flow, while at high velocity sites (0.20 ± 0.01

524   ms^{-1}), the threshold patch length was 0.9 m. They also found fine sediment accumulation within

525   patches was dependent on the velocity of the ambient flow field. Our findings corroborate this

526   relationship between sediment patterns and patch length, as deposited sediment increased as

527   the length of the patches increased, and extends it to turbidity currents as well as the river flow

528   studied by Schoelynck et al. (2012) and Licci et al. (2019). Our experiments also support the

529 theory that normalized depositional flux rates of sediment are greater in dense patches than in

530 sparse ones, regardless of particle size. In the context of turbidity currents, a threshold value has

531 been found, such that for patches smaller than 20±2 times the water depth, dependency with

532 patch length disappears and sediment deposition rates depend only on the vegetation density.

533

534 **5.   Conclusions**

535

536 Laboratory flume experiments have been reported which, for the first time, investigate (a) the

537 effects of varying water depth on the passage of turbidity currents through continuous arrays of

538 obstacles; and (b) the effects of finite-length arrays of obstacles on the hydrodynamics and

539 patterns of sediment deposition of turbidity currents, compared to those of continuous, quasi-

540 infinite obstacle arrays. Our interest lies primarily in contexts where the obstacle arrays are

541 aquatic vegetation canopies, but they can equally be taken to simulate other natural or built

542 phenomena. The patch lengths studied were of the same order of magnitude as the length scales

543 over which the turbidity currents develop and decay, allowing the influence of patches on these

544 processes to be elucidated. We varied patch length, canopy density and water height, but did not

545 vary either the initial sediment concentration of the turbidity current fluid, or the physical properties

546 of the material used to simulate the canopy vegetation, so the reported findings do not speak to

547 the possible effects of these last two factors.

548

549 We found that the influence of the vegetation patches on turbidity currents is parameterised by

550 two non-dimensional variables: the canopy's frontal area density, aH, and the patch's aspect ratio

551 with respect to the water depth, L_{patch}/H. We found strong relationships between these two

552 parameters and (i) the downstream distances at which the currents transition from an inertial

553 regime to a drag-dominated regime; and (ii) the rate of depositional sediment flux from the current

554 to the bed, and the ratio of values of this flux for fine and coarse sediment fractions. The transition

555 distances, normalized by water depth, are found to follow a power law relationship with aH and

556 L_{patch}/H, which is independent of the dynamical state of the current at the point where it emerges

557 from the patch. The depositional flux rates for fine and coarse sediment fractions, normalised by

558 the canopy density, DF/aH, are both found to be constant for $L_{patch}/H < 20±2$, with the value for

559   fine sediment greater than that for coarse sediment by a factor of 1.60. For $L_{patch}/H > 20\pm2$, the

560   value of DF/aH increases with L_{patch}/H, i.e. the rate of deposition is greater for any given canopy

561   density than it would be in patches shorter than $20\pm2H$. If we consider vegetation canopy density

562   values typically found in nature and typical shallow water depths of order 0.1-1 m, the patch sizes

563   at which these thresholds in influence occur are of the order of tens of centimetres to a few metres,

564   which are typical sizes of vegetation patches found in many freshwater and coastal marine

565   contexts. Thus, the results presented here are highly relevant to understanding the interactions

566   of turbidity currents with vegetation in natural environments.

567

568   **Acknowledgments**

569

573

574   **References**

575

576   Adam, P., 2002. Saltmarshes in a time of change. Environmental Conservation, 29: 39-61

577

578   Adhitya, A., Bouma, T.J., Folkard, A.M., van Katwijk, M.M., Callaghan, D.P., de Iongh, H.H.,

579   Herman, P.M.J., 2014. Comparison of the influence of patch-scale and meadow-scale

580   characteristics on flow within seagrass meadows: a flume study. Marine Ecology Progress Series,

581   516: 49-59

582

583   Agawin, N.S.R., Duarte, C.M., 2002. Evidence of direct particle trapping by a tropical seagrass

584   meadow. Estuaries and Coasts, 25: 1205-1209 https://doi.org/10.1007/BF02692217

585

586   Benjamin, T.B., 1968. Gravity currents and related phenomena. Journal of Fluid Mechanics, 31:

587   209-248

588

589   Bhaganagar, K., 2014. Direct numerical simulation of lock-exchange density currents over the

590   rough wall in slumping phase. Journal of Hydraulic Research, 52: 386-398

591

592   Blott, S.J., Pye, K., 2012. Particle size scales and classification of sediment types based on

593   particle distributions: review and recommended procedures. Sedimentology, 59: 2071–2096

594

595   Bonnecaze, R.T., Huppert, H.E., Lister, J.R., 1993. Particle-driven gravity currents. Journal of

596   Fluid Mechanics, 250: 339-369

597

598   Bouma, T.J., Van Duren, L.A., Temmerman, S., Claverie, T., Blanco-Garcia, A., Ysebaert, T.,

599   Herman, P.M.J., 2007. Spatial flow and sedimentation patterns within patches of epibenthic

600   structures: Combining field, flume and modelling experiments. Continental Shelf Research, 27:

601   1020-1045

602

603   Bouma, T.J., Friedrichs, M., Van Wesenbeeck, B.K., Temmerman, S., Graf, G., Herman, P.M.J.,

604   2009. Density-dependent linkage of scale-dependent feedbacks: a flume study on the intertidal

605   macrophyte *Spartina anglica*. Oikos, 118: 260-268. https://doi.org/10.1111/j.1600-

606   0706.2008.16892.x

607

608   Bouma, T.J., Temmerman, S., Van Duren, L.A., Martini, E., Vandenbruwaene, W., Callaghan,

609   D.P., Balke, T., Biermans, G., and others, 2013. Organism traits determine the strength of scale-

610   dependent bio-geomorphic feedbacks: A flume study on three intertidal plant species.

611   Geomorphology, 180-181: 57-65.

612

613   Colomer, J., Soler, M., Serra, T., Casamitjana, X., Oldham, C., 2017. Impact of anthropogenically

614   created canopy gaps on wave attenuation in a *Posidonia oceanica* seagrass meadow. Marine

615   Ecology Progress Series, 569: 103-116

616

617   Cotton, J., Wharton, G., Bass, J., Heppell, C., Wotton, R., 2006. The effects of seasonal changes

618   to in-stream vegetation cover on patterns of flow and accumulation of sediment. Geomorphology,

619   77: 320-334

620

621   Di Carlo G., Badalamenti, F., Jensen, A.C., Koch, E.W., and Riggio, S., 2005. Colonisation

622   process of vegetative fragments of *Posidonia oceanica* (L.) Delile on rubble mounds. Marine

623   Biology, 147: 1261-1270. https://doi.org/10.1007/s002277-005-0035-0

624

625   Dwirea, K.A., Mellmann-Brown, S., Gurrieri, J.T., 2018. Potential effects of climate change on

626   riparian areas, wetlands, and groundwater-dependent ecosystems in the Blue Mountains,

627   Oregon, USA. Climate Services, 10: 44-52

628

629   El Allaoui, N., Serra, T., Soler, M., Pujol, D., Oldham, C., 2015. Modified hydrodynamics in

630   canopies with longitudinal gaps exposed to oscillatory flows. Journal of Hydrology, 531: 840-849

631

632   El Allaoui, N., Serra, T, Colomer, J., Soler, M., Casamitjana, X., Oldham, C., 2016. Interactions

633   between fragmented seagrass canopies and the local hydrodynamics, PLoS ONE, 11: 5.

634   https://doi.org/10.1371/journal.pone.0156264

635

636   Felix, M., 2002. Flow structure of turbidity currents. Sedimentology, 49: 397-419

637

638   Folkard, A.M., 2005. Hydrodynamics of model *Posidonia oceanica* patches in shallow water.

639   Limnology and Oceanography, 50: 1592-1600. https://doi.org/10.4319/lo.2005.50.5.1592

640

641   Folkard, A.M., 2019. Biophysical interactions in fragmented canopies: fundamental processes,

642   consequences, and upscaling, Frontiers in Marine Science, 6.

643   https://doi.org/10.3389/fmars.2019.00279.

644

645 Francisco, E.P., Espath, L.F.R., Laizet, S., Silvestrini, J.H., 2017. Reynolds number and settling

646 velocity influence for finite-release particle-laden gravity currents in a basin. Computational

647 Geosciences, 110: 1-9

648

649 Ghisalberti, M., Nepf, H.M., 2004. The limited growth of vegetated shear layers, Water Resoures

650 Research, 40: W07502. https://doi.org/10.1029/2003WR002776

651

652 Gillis, L.G., Maza, M., Argemi, M., Balke, T., Folkard, A.M., Garcia-Maribona, J., Geng, L.,

653 Lanzoni, S., Meire, D., Paul, M., Sgarabotto, A., Suzuki, T., Lara, J.L., 2019. Plant effects on

654 hydrodynamics and sedimentation at coastal wetland edges. Proceedings of the HYDRALAB+

655 Joint User Meeting, Bucharest, May 2019

656

657 Gladstone, C., Phillips, J.C., Sparks, R.S.J., 1998. Experiments on bidisperse, constant-volume

658 gravity currents: propagation and sediment deposition. Sedimentology, 45: 833-843

659

660 Gonzalez-Juez, E., Meiburg, E., Tokyay, T., Constantinescu, G., 2010. Gravity current mixing in

661 gravity currents propagating up mild slopes flow past a circular cylinder: forces, wall shear

662 stresses and implications for scour. J. Fluid Mech. 649: 69-102.

663

664 Gurnell, A., 2014. Plants as river system engineers, Earth Surf. Process. Landforms. 39: 4-25.

665

666 Harris, T.C., Hogg, A.J., Huppert, H., 2002. Polydisperse particle-driven gravity currents. J. Fluid

667 Mech. 472: 333-371

668

669 Hatcher, L., Hogg, A.J., Woods, A.W., 2000. The effect of drag on turbulent gravity currents. J.

670 Fluid Mech. 416, 297-314.

671

672 Huppert, H. E., Simpson, J. E., 1980. The slumping of gravity currents. J. Fluid Mech., 99: 785-

673 799.

674

675 La Rocca, M., Adduce, C., Sciortino, G., Pinzon, A.B., 2008. Experimental and numerical

676 simulation of three-dimensional gravity currents on smooth and rough bottom. Phys. Fluids 20:

677 106603. https://doi.org/10.1063/1.3002381

678

679 Licci, S., Nepf, H., Delolme, C., Marmonier, P., Bouma, T.J., Puijalon, S., 2019. The role of patch

680 size in ecosystem engineering capacity: a case study of aquatic vegetation. Aquatic Sciences,

681 81: 41. https://doi.org/10.1007/s00027-019-0635-2

682

683 Liu, C., Nepf, H., 2015. Sediment deposition within and around a finite patch of model vegetation

684 over a range of channel velocity. Water Resources Research., 52, 600-612,

685 https://doi.org/10.1002/2015WR018249

686

687 Lowe, B.J., Watts, R.J. Roberts, J., Robertson, A., 2010. The effect of experimental inundation

688 and sediment deposition on the survival and growth of two herbaceous riverbank plant species.

689 Plant Ecol. (2010) 209:57–69. https://doi.org/10.1007/s11258-010-9721-1

690

691 Ludwig, J.A., Wilcox, B.P., Breshears, D.D., Tongway, D.J., Imeson, A.C. 2005. Vegetation

692 patches and runoff-erosion as interacting ecohydrological processes in semiarid landscapes.

693 Ecology, 86(2), 288-297

694

695 Madsen JD, Chambers PA, James WF, Koch EW, Westlake DF. 2001. The interaction between

696 water movements, sediment dynamics and submersed macrophytes. Hydrobiologia 444: 71-84.

697

698 Mandal S, Maiti R. 2015. Semi-quantitative Approaches for Landslide Assessment and Prediction.

699 Springer Natural Hazards. Springer: Berlin.

700

701 Manners, R.B., Wilcox, A.C., Kui, L., Lightbody, A.F., Stella, J.C., Sklar, L.S. 2015. When do

702 plants modify fluvial processes ? Plant-hydraulic interactions under variable flow and sediment

703 supply rates. J. Geophys. Res.Earth Surf., 120, 325-345. https://doi.org/10.1002/2014jf003265.

704

705 Maxworthy T, Leilich J, Simpson JE, Meiburg EH. 2002. The propagation of a gravity current in a

706 linearly stratified fluid. J. Fluid Mech. 453: 371-394.

707

708 Montakhab A, Yusuf B, Ghazali AH, Mohamed TA. 2012. Flow and sediment transport in

709 vegetated waterways: a review. Rev. Environ. Sci. Biotechnol. 11: 275–287.

710

711 Nardin, W., Locatelli, S., Pasquarella, V., Rulli, M.C., Woodcock, C.E., Fagherazzi, S., 2016.

712 Dynamics of a fringe mangrove forest detected by landsat images in the Mekong river delta.

713 Vietnam. Earth Surf. Process. Landf. 41, 2024-2037.

714 https://doi.org/10.1080/00221686.2012.696559.

715

716 Nepf, H.M., 1999. Drag, turbulence, and diffusion in flow through emergent vegetation. Water

717 Resour. Res. 35(2): 479-489.

718

719 Nepf, H.M., 2012. Flow and transport in regions with aquatic vegetation. Annual Review of Fluid

720 Mechanics, 44:123-142. https://doi.org/10.1146/annurev-fluid-120710-101048

721

722 Nogueira HIS, Adduce C, Alves E, Franca MJ. 2013. Analysis of lock-exchange gravity currents

723 over smooth and rough beds. J. Hydraul. Res. 51(4): 417-431.

724

725 Nogueira HIS, Adduce C, Alves E, Franca MJ, 2014. Dynamics of the head of gravity currents.

726 Environ. Fluid. Mech. 14: 519-540.

727

728 Pujol, D., Colomer, J., Serra, T., Casamitjana, X., 2010. Effect of submerged aquatic vegetation

729 on turbulence induced by an oscillating grid. Continental Shelf Research 30: 1019-1029

730

731 Pujol, D., Serra T., Colomer J., Casamitjana X., 2013. Flow structure in canopy models dominated

732 by progressive waves. J. Hydrology 486: 281-292.

733

734 Richardson, D.M., Holmes, P.M., Esler, K.J., Galatowitsch, S.M., Stromberg, J.C., Kirkman, S.P.,

735 Pysek P., Hobbs, R.J. 2007. Riparian vegetation: degradation, alien plant invasions, and

736 restoration prospects. Diversity and Distributions, 13, 126–139

737

738 Rietkerk, M., van de Koppel, J., 2008. Regular pattern formation in real ecosystems. Trends in

739 Ecology and Evolution, 23: 169-175

740

741 Schoelynck, J., De Groote, T., Bal, K., Vandenbruwaene, W., Meire, P., Temmerman, S. 2012.

742 Self-organised patchiness and scale-dependent bio-geomorphic feedbacks in aquatic river

743 vegetation. Ecography, 35, 760–768. https://doi.org/10.1111/j.1600-0587.2011. 07177.x

744

745 Schulze, D. Rupprecht, F. Nolte, S., · Jensen, K. 2019. Seasonal and spatial within-marsh

746 differences of biophysical plant properties: implications for wave attenuation capacity of salt

747 marshes. Aquatic Sciences 81 (4). https://doi.org/10.1007/s00027-019-0660-1

748

749 Serra, T., Colomer, J., Gacia, E., Soler, M., Casamitjana, X., 2002. Effects of a turbid

750 hydrothermal plume on the sedimentation rates in a karstic lake. Geophys. Res. Lett., 29: DOI:

751 10.1029/2002GL015368.

752

753 Serra, T., Soler, M., Julia, R., Casamitjana, X., Colomer, J., 2005. Behaviour and dynamics of a

754 hydrothermal plume in Lake Banyoles, Catalonia, NE Spain. Sedimentology, 52: 795-808

755

756 Serra T, Colomer J, Oldham, C., 2018. Local hydrodynamics at edges of marine canopies under

757 oscillatory flows. Plos One, 13, 8. https://doi.org/10.1371/journal.pone.0201737

758

759 Shin JO, Dalziel SB, Linden PF. 2004. Gravity currents produced by lock exchange. J. Fluid Mech.

760 521: 1–34. https://doi.org/10.1017/S002211200400165X

761

762 Simpson JE. 1982. Gravity currents in the laboratory, atmosphere, and ocean. Annu. Rev. Fluid

763 Mech. 14:213-234.

764

765 Soler M, Colomer J, Serra, T., Casamitjana, X., Folkard, A. M., 2017. Sediment deposition from

766 turbidity currents in simulated aquatic vegetation canopies. Sedimentology 64: 1132–1146.

767

768 Soler, M., Colomer, J., Folkard, A.M., Serra, T., 2020. Particle size segregation of turbidity current

769 deposits in vegetated canopies. Science of Total Environment,

770 https://doi.org/10.1016/j.scitotenv.2019.134784

771

772 Tamburello, L., Benedetti-Cecchi, L., Ghedini, G., Alestra, T., Bulleri, F. (2012) Variation in the

773 structure of subtidal landscapes in the NW Mediterranean Sea. Marine Ecology Progress Series,

774 457, 29-41.

775

776 Tanino Y, Nepf HM, Kulis PS. 2005. Gravity currents in aquatic canopies. Water Resour. Res.

777 41:W12402. https://doi.org/10.1029/2005WR004216

778

779 Van Rijn LC. 2007. Unified view of sediment transport by currents and waves I: Initiation of motion,

780 bed roughness, and bed-load transport. J. Hydraul. Eng. 133: 649–667.

781

782 Vandenbruwaene, W., Temmerman,S., Bouma, T.J., Klaassen, P.C., de Vries, M.B., Callaghan,

783 D.P., van Steeg, P., Dekker, F. van Duren, L.A., Martini, E. , T. Balke, T., Biermans, G.

784

785 White FM. 1991. Viscous Fluids Flow, 2nd ed., McGraw-Hill: New York.

786

787 Xiu, L., Yan, C., Li, X., Qian, D., Feng, K. 2019. Changes in wetlands and surrounding land cover

788 in a desert area under the influences of human and climatic factors: A case study of the Hongjian

789 Nur region. Ecological Indicators 101: 261-273

790

791 Zhang X, Nepf, HM. 2008. Density-driven exchange flow between open water and aquatic

792 canopy. Water Resour. Res. 44: W08417, https://doi.org/10.1029/2007WR006676

793

794   Zhang, X., Nepf, H.M., 2011. Exchange flow between open water and floating vegetation. Environ

795   Fluid Mech., 11: 531-546

796

797   Zhang X, Tang, C., Nepf, HM. 2018.Turbulent Kinetic Energy in Submerged Model Canopies

798   Under Oscillatory Flow. Water Resources Research 54: https://doi.org/10.1002/2017WR021732

799

800   Zong L, Nepf HM. 2010. Flow and deposition in and around a finite patch of vegetation.

801   Geomorphology 116, 363-372. https://doi.org/10.1016/j.geomorph.2019.11.020.

802

803 **Captions to tables and figures**

804

805 Table 1: Summary of gravity current hydrodynamics, showing the time dependency of the position

806 of the current toe, x_c, depending on the density-varying agent and the existence or absence of

807 obstacles.

808

809 Table 2: Summary of experimental conditions (water depth, H; vegetation density, expressed as

810 *SPF*, *a* and *ad*; vegetation patch length, L_{patch}) and non-dimensional parameter values (vegetation

811 frontal area, *aH*; canopy aspect ratio, L_{patch}/H) for each experimental run.

812

813 Figure 1: (A) Side view of the laboratory flume, which is divided by a removable, sealing partition

814 (lock gate) into two sections. The smaller, left-hand, section is a reservoir for preparation of the

815 turbidity current fluid. The right-hand section contains the simulated vegetation and is the

816 experimental test section. The vertical coordinate is z, with z = 0 at the bed (increasing upwards);

817 the longitudinal coordinate is x, with x = 0 at the lock gate (increasing to the right); (B) Side view

818 of the laboratory flume when the turbidity current (shaded) is flowing through a vegetation patch

819 of length L_{patch}; (C) Top view of the laboratory flume, with a vegetation patch in the test section,

820 showing the locations of fourteen sediment traps (ST0 to ST13) on the flume bed. ST0 is 20 cm

821 to the left of the lock gate, ST1 is 20 cm to the right of the lock gate, and each subsequent trap is

822 a further 20 cm to the right. The canopy is a randomly-distributed array of obstacles with solid

823 plant fraction (SPF) values of 1.0, 2, 2.5, 3, 3.5 and 4%.

824

825 Figure 2: Particle size distribution of the turbidity current sediments, expressed in terms of mass

826 per unit volume (gL^{-1}). The distribution is divided into fine (2.5 μm < d < 6.2 μm) and coarse (6.2

827 μm < d < 104.0 μm) fractions.

828

829 Figure 3: Temporal evolution of the turbidity current toe for fully-vegetated runs carried out using

830 different vegetation canopy densities and the non-vegetated case.

831

832 Figure 4: (A) Plot of the temporal evolution of the turbidity current toe for Run 6 (H = 12 cm, SPF

833 = 3.5%). The three hydrodynamic regimes can be distinguished by their different slopes: 1 for the

834 inertial regime, 1/2 for the drag-dominated regime and 1/5 for the viscous regime. The transition

835 zones between these regimes are indicated by grey zones. (B) Plot of normalised toe drag,

836 $C_{Da}ax_c$, versus the non-dimensional frontal canopy area, aH, showing values at which the drag-

837 dominated regime begins ($C_{Da}aL_{ini}$) and ends ($C_{Da}aL_{end}$). Data are from Runs 2-7 (H = 12cm, SPF

838 = 1 to 4%) (circles), and from Runs 8-11 (SPF = 4%, H = 3, 6, 9, 12 and 15 cm) (squares). Dashed

839 lines represent the linear best fit of the data. The grey area indicates the drag-dominated regime.

840

841 Figure 5: Plot of the temporal evolution of the current toe position, x_c, for vegetation patches with

842 a water height H = 6 cm, SPF = 4% and a patch length L_{patch} of (A) 60 cm (10H); (B) 92 cm (15.3H,

843 black circles) and (C) 116 cm (19.3H, white circles). The inertial regime ends downstream of the

844 patch in (A), but within it in cases shown in (B) and (C). The three hydrodynamic regimes that the

845 current passes through in each case are shown. Note that in (A) the inertial regime transitions to

846 a self-similar regime ($x_c \propto t^{2/3}$), whereas in (B) and (C) it transitions to a drag-dominated regime

847 ($x_c \propto t^{1/2}$).

848

849 Figure 6. Plot of the current toe position at which the drag-dominated regime begins, L_{ini}, non-

850 dimensionalized by water height H, against the function of aH and L_{patch}/H shown in Equation 3.

851 Data from all experimental runs using both fully-vegetated (black circles) and vegetation patch

852 (white circles) configurations are shown. The dashed line illustrates the power best fit ($\sim A \cdot x^B$) of

853 the data with A = 3.72; B=-0.77, r^2 = 0.95; n = 23; p<<0.01.

854

855 Figure 7: Ratio of the non-dimensional depositional sediment flux, DF, to the canopy frontal area

856 aH at sediments traps located near the centre of the drag-dominated regime for each run, plotted

857 against the canopy aspect ratio, L_{patch}/H for (A) fine particles and (B) coarse particles. The plots

858 are divided into two zones denoting the difference in behaviour that depends on whether L_{patch}/H

859 is greater or less than 20 ± 2. The lines illustrate the linear best fits of the data with the right hand

860 sections of each one having: (a) m = 0.039, r^2 = 0.80, n = 28, p<<0.01; and (b) m = 0.022, r^2 =

861 0.83, n = 31, p<<0.01. Data shown for all runs: fully-vegetated runs with canopy frontal areas, aH,

862   smaller than 0.8 (black circles) and greater than 0.08 (black triangles), and vegetation patch runs

863   with canopy frontal areas smaller than 0.8 (white circles) and greater than 0.08 (white triangles).

864

A) Side view (Full vegetated)

CCD moving Camera

Lockgate

C_o

30cm

H

ST0   ST1 ST2 ST3 ST4 ST5 ST6 ST7 ST8 ST9 ST10 ST11 ST12 ST13

134 cm

20 cm

266 cm

x (longitudinal axis)

B) Side view (Vegetation patch)

z   CCD moving Camera

Lockgate

C_o

30cm

H

L_{patch}

x (longitudinal axis)

C) Top view (Vegetation Patch)

y (transversal axis)

C_o

30cm

L_{patch}

x (longitudinal axis)

Fig 1

865

866

32
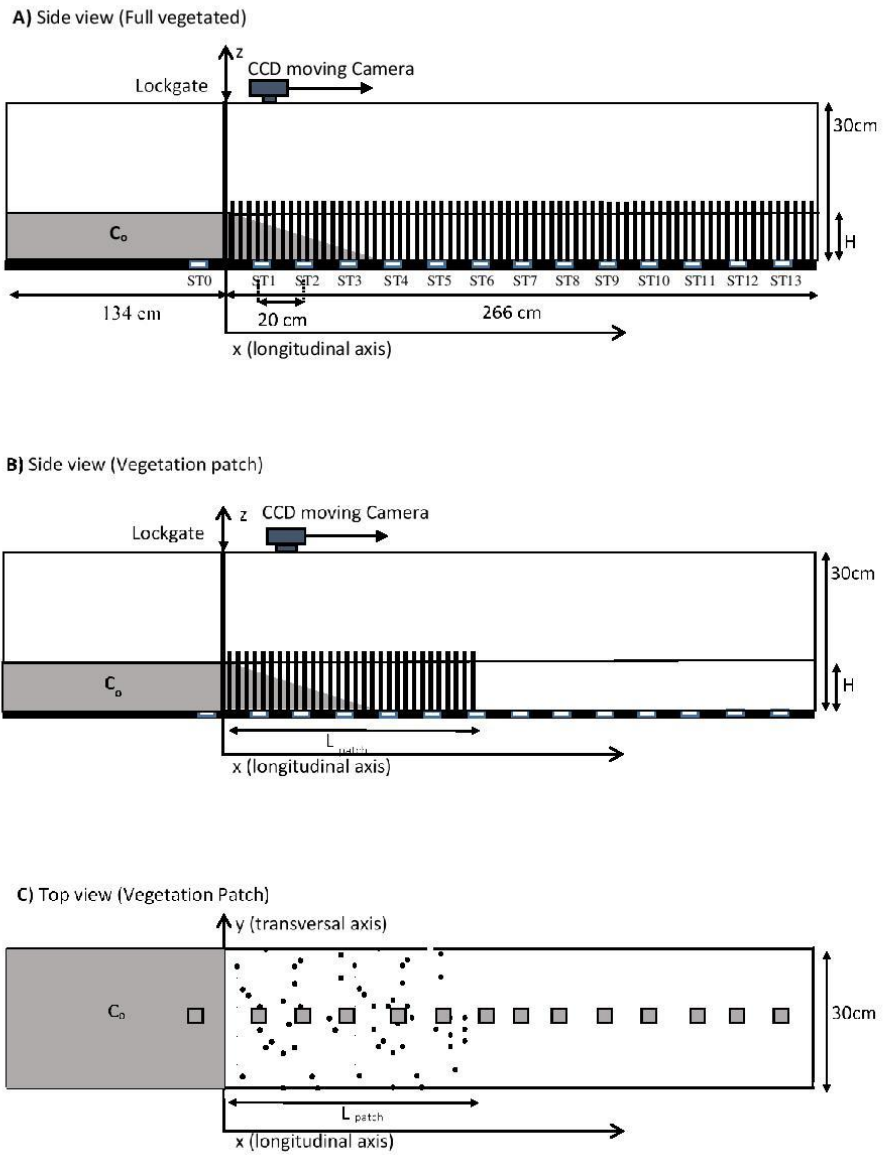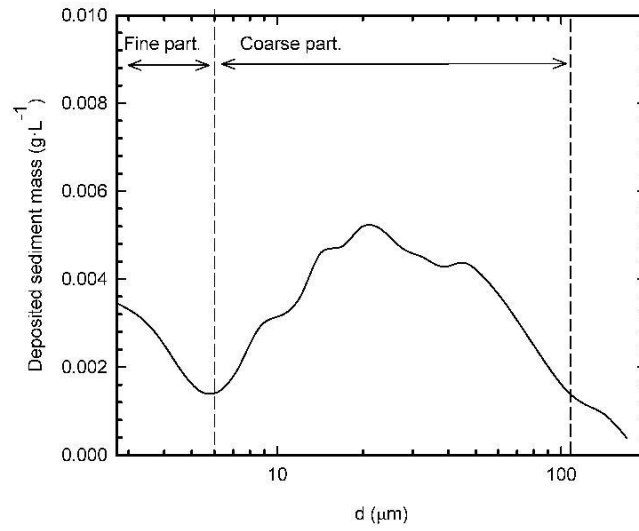
Fig.2

867

868

Fig. 3

869

870

A)

B)

Fig4

871

872
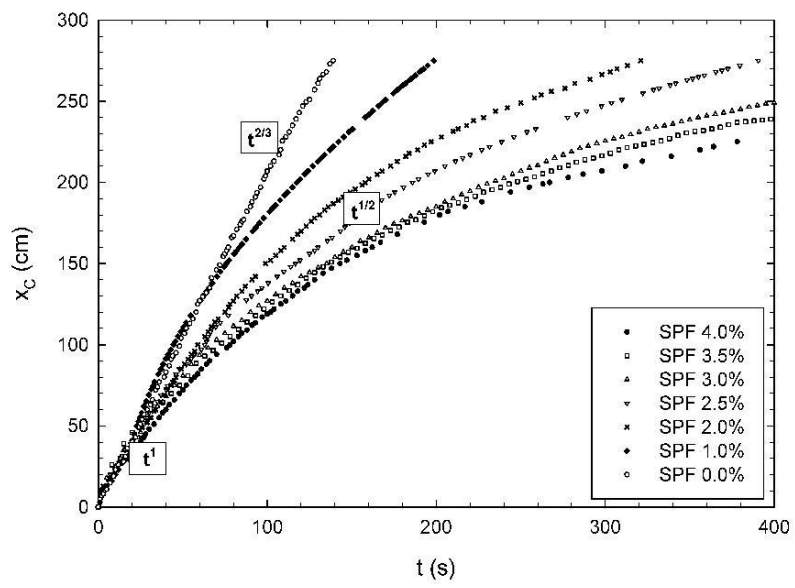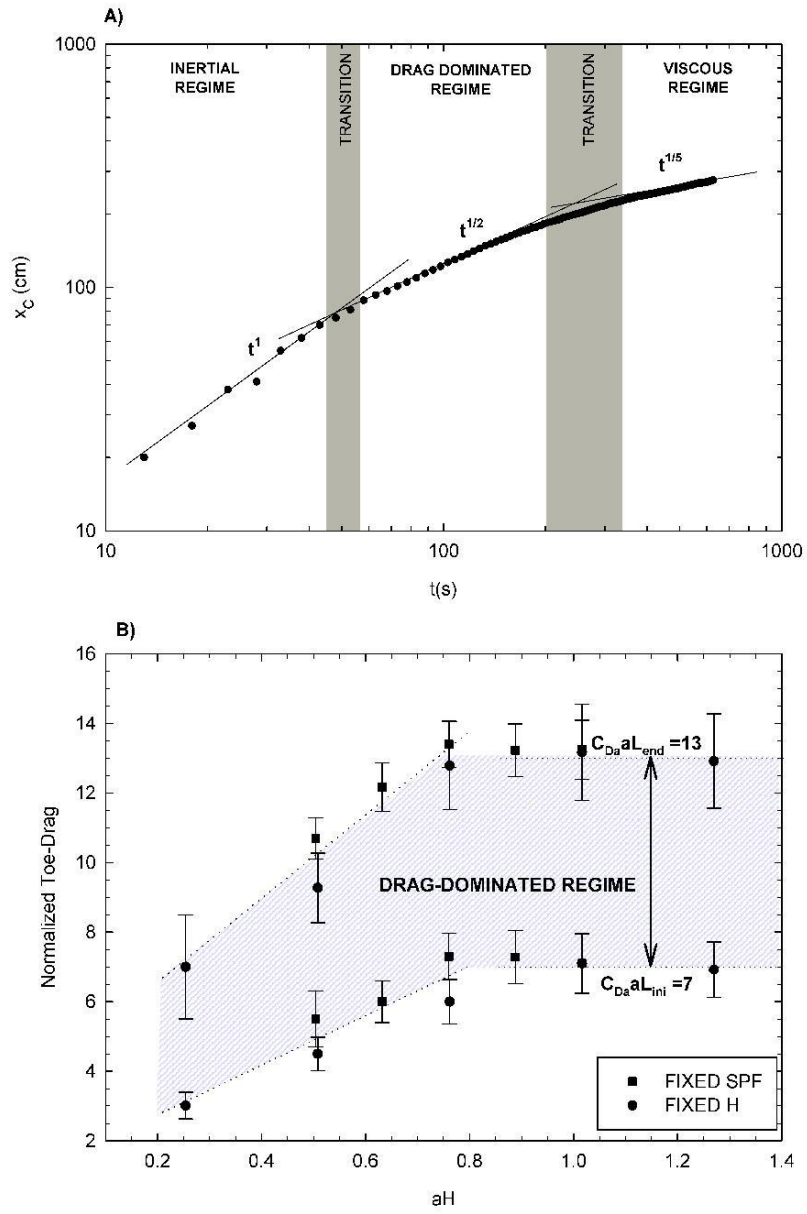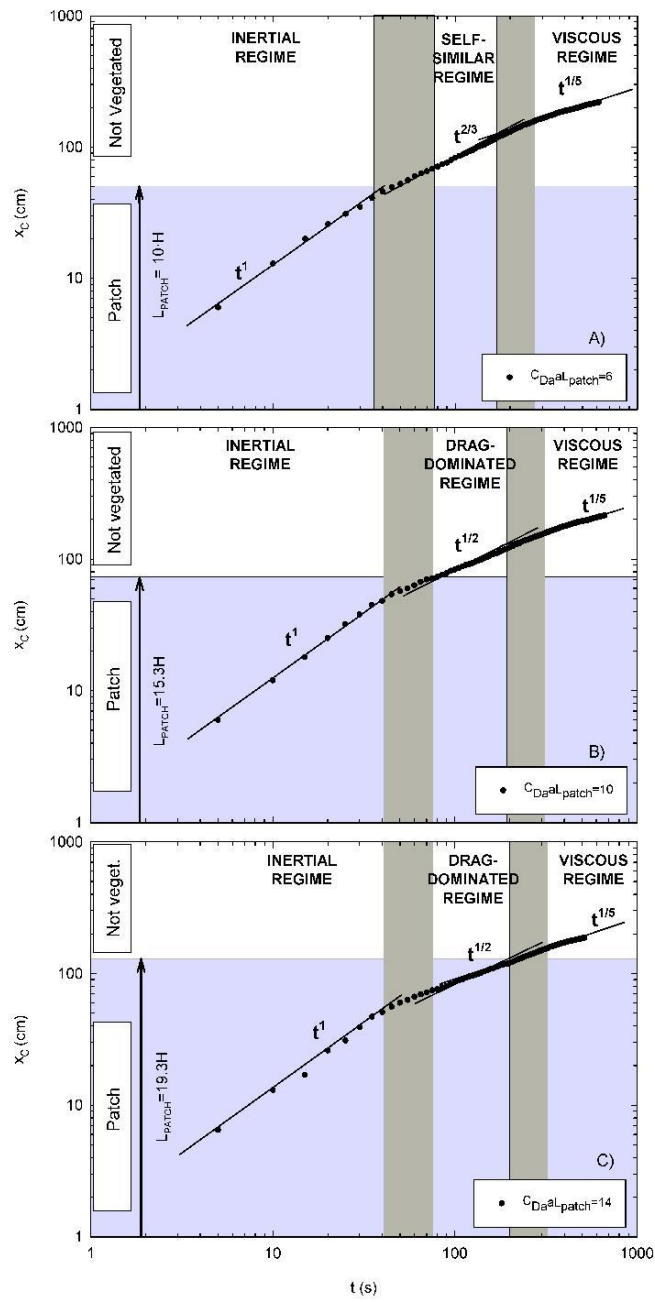
Fig.5
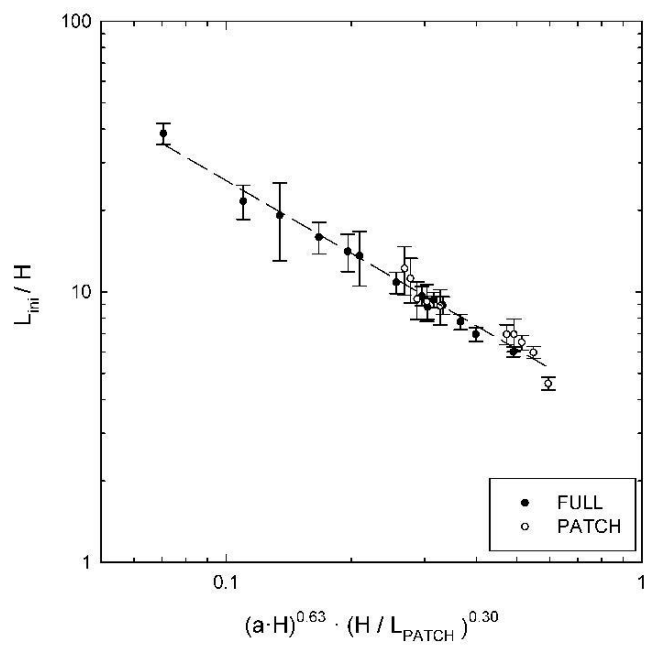
Fig.6

875

876

877

878

879

880

881

882

	Density varying agent	volume release	Regime		
			Inertial	Self-similar	Viscous
Without obstacles	conservative (heat, salinity)	Infinite	$x_c \sim t^1$	⟋	$x_c \sim t^{1/5}$
		Finite		$x_c \sim t^{1/2}$	
	not conservative (particles suspension)	Finite		$x_c \sim t^{2/3}$	
			Inertial	Drag-dominated	Viscous
With obstacles	conservative (heat, salinity)	Finite	$x_c \sim t^1$	$x_c \sim t^{1/2}$	$x_c \sim t^{1/5}$
	not conservative (particles suspension)	Finite		$x_c \sim t^{1/2}$	

883

884

885   Table 1

886

FULL VEGETATED EXPERIMENTS							
exp.	H (cm)	SPF (%)	Lpatch (cm)		a (m^{-1})	aH	ad
1	12	0	0		0	0	0
2		1	280 (Full)		2.13	0.26	0.013
3		2			4.20	0.50	0.025
4		2.5			5.27	0.63	0.032
5		3			6.33	0.76	0.038
6		3.5			7.40	0.89	0.044
7		4			8.47	1.02	0.051
8	15	4	280 (Full)		8.47	1.27	0.051
9	9					0.76	
10	6					0.51	
11	3					0.25	
12	15	2	280 (Full)		4.20	0.63	0.025
13	9					0.38	
14	6					0.25	
15	3					0.13	
VEGETATED PATCHS EXPERIMENTS							
exp.	H (cm)	SPF (%)	Lpatch (cm)	$C_D \cdot a \cdot Lpatch$	a (m^{-1})	aH	ad
16	6	4	116	14	8.47	0.51	0.051
17			104	12			
18			92	10			
19			77	8			
20			60	6			
21	12	4	151	14	8.47	1.02	0.051
22			132	12			
23			113	10			
24			92	8			
25			70	6			

889

890   Table 2

891